Iron-mediated interaction of alpha synuclein with lipid raft model membranes†

Fabio Perissinotto, [a] Chiaramaria Stani, [a] Elena De Cecco, [b] Lisa Vaccari, [a] Valeria Rondelli, [c] Paola Posocco, [d] Pietro Parisse, [a] Denis Scaini, *[a,b] Giuseppe Legname [a,b] and Loredana Casalis *[a]

The aberrant misfolding and aggregation of alpha synuclein (αS) into toxic oligomeric species is one of the key features associated with the pathogenesis of Parkinson's disease (PD). It involves different biochemical and biophysical factors as plasma membrane binding and interaction with heavy metal ions. In the present work, atomic force microscopy (AFM) is combined with Fourier Transform Infrared Spectroscopy (FTIR) measurements to investigate the interaction of *wild-type* (WT) and A53T mutated alpha synuclein with artificial lipid bilayers mimicking lipid raft (LR) domains, before and after ferrous cations (Fe^{2+}) treatment. In the absence of iron, protein monomers produce a thinning of the membrane, targeting the non-raft phase of the bilayer preferentially. On the contrary, iron actively promotes the formation of globular protein aggregates, resembling oligomers, targeted to LR domains. In both aggregation states, monomer and oligomer, the mutated A53T protein exhibits a greater and faster membrane-interaction. These results underlie a new mechanism of membrane-protein interaction in PD. The targeting of Fe^{2+}-promoted αS oligomers to LRs might be functional for the disease and be helpful for the development of new therapeutic strategies.

Introduction

Parkinson's disease (PD) is a neurodegenerative synucleinopathy characterized by the degeneration of dopaminergic and noradrenergic neurons of *substantia nigra pars compacta* (SNPC) in the brain.[1] Despite the lack of a comprehensive mechanism that triggers the pathology, the main hallmark of PD is the presence of Lewy bodies, which are abnormal cytosolic depositions of alpha synuclein (αS) aggregates, iron and other ubiquitinated proteins.[2] αS is a 140 amino acids intrinsically-disordered protein mainly localized in neuronal presynapses.[3] The protein is characterized by three distinct regions: the N-terminal domain (residues 1–60), composed of imperfect repetitions of the hexamer KTKEGV which anchors the protein to biological membranes leading to a protein structural rearrangement into α-helix conformation;[4,5] the central hydrophobic domain (NAC, residue 61–95) involved in αS aggregation and formation of amyloid structures;[6,7] the C-terminal tail (residues 96–140) which is rich in acidic amino acids and regulates fibrillization.[8] The primary biological function attributed to αS is the binding to the synaptic membrane to regulate the homeostasis of presynaptic vesicles modulating the neurotransmitter release at neuron terminals.[9–11] The protein is assumed to bind membrane vesicles in correspondence of specific membrane microdomains called lipid rafts (LRs), promoting synaptic localization and its physiological activity.[12] One of the key molecular events involved in the pathogenesis of PD is the aberrant misfolding and aggregation of αS, resulting in both intracellular and extracellular accumulation of distinct species in the brain: oligomers, intermediate products of the αS aggregation pathway, and fibrils.[13] These protein aggregates have been shown to interact intracellularly with hippocampal cell membranes leading to a 5-fold increase of membrane conductance and a 2.5 fold-increase of synaptic transmission.[14] At the same time, the extracellular accumulation of αS plays a crucial role in triggering the cell-to-cell spreading of the disease.[15] Although recent findings point to αS prefibrillar oligomers rather than to amyloid fibrils as the main toxic species[16,17] promoting the development of PD, the biological mechanisms that induce aggregation and neurotoxicity are still controversial.[18] αS oligomers have been shown to promote cell membrane destabilization and permeabilization,[19,20]

[a]*Elettra Sincrotrone Trieste S.C.p.A., 34149 Trieste, Italy. E-mail: dscaini@sissa.it, loredana.casalis@elettra.eu*
[b]*Department of Neuroscience, Scuola Internazionale Superiore di Studi Avanzati (SISSA), 34136 Trieste, Italy*
[c]*Department of Medical Biotechnology and Translational Medicine, Università degli Studi di Milano, 20090 Segrate, Italy*
[d]*Department of Engineering and Architecture, University of Trieste, 34127 Trieste, Italy*
†Electronic supplementary information (ESI) available. See DOI: 10.1039/d0nr00287a

leading to calcium flux alteration, dispersion of intra-vesicular dopamine and depolarization of mitochondrial membrane.[21–24] Many possible causes of oligomerization or/and amyloid structures formation have been proposed from *in vivo* and *in vitro* models. Genetic point mutations as well as a combination of several environmental and physicochemical factors like metal cations, anionic molecules, local change of pH, interaction with other proteins and small molecules are known to dramatically affect αS propensity to aggregate.[25–27] Genetic point mutations of the αS-codifying gene SNCA associated with cases of inherited PD produce the mutated forms known as A53T, A30P and E46K,[28] which display different aggregation kinetics and pathological aggressiveness compared to the *wild-type* (WT) αS.[17,29,30] Some recent studies focused on the relationship between PD progression and the accumulation of biologically relevant metal ions as iron and copper.[31–34] Abnormal concentrations of these metals have indeed been discovered in the brain of PD patients.[35–37] Moreover, several metal-binding sites are known to be present at the αS C-terminal domain promoting the *in vitro* formation of stable protein-metal complexes.[38,39] Particularly interesting it is the role of iron's redox chemistry. Iron accumulation triggers oxidative stress by reactive oxygen species (ROS) production. This leads to lipid and nucleic acid modifications, mitochondrial dysfunctions and protein aggregation, as in the case of αS.[40] Such changes may result in neurological diseases. However, it is not yet clear whether iron triggers αS aggregation or if increased protein levels lead to iron accumulation. Higher iron levels have been measured in neurons over-expressing αS compared to the ones normally expressing the protein.[41] A detailed molecular description of membrane-αS interaction in the presence of iron ions would improve our understanding of the onset and progression of PD (as well as of other synucleinopathies) and would provide new tools for developing therapeutic strategies against these diseases. Here, by precise atomic force microscopy (AFM) imaging and Fourier Transform Infrared Spectroscopy in Attenuated Total Reflection mode (FTIR-ATR), we investigated the role of iron in inducing αS aggregation and specific membrane-binding interactions on lipid bilayer model systems. In particular, we compared the behavior of WT and A53T αS, whose point mutation at residue 53 (Ala replaced by Thr) affects its membrane binding capability. A53T is known to display accelerated aggregation kinetics then WT αS as well as higher iron-induced aggregation and toxicity in cellular systems. *In vitro* exposure of neurons to high levels of ferrous ions (Fe^{2+}) has been shown to stimulate the formation of αS aggregates with a stronger effect on A53T-expressing cell lines than on WT αS ones.[42] For a more comprehensive assessment of αS-membrane interaction, the artificial system we created was endowed with raft-like microdomains to mimic the composition and morphology of the neuronal cell membrane. First, from *in vitro* protein-aggregation assays we assessed the role of iron in the dynamics of protein oligomers formation. Then we demonstrated that iron modifies the interaction of the two protein species with model lipid bilayers, targeting αS to LR domains and promoting the formation of aggregates whose structure is dependent on the specific protein–lipid interaction. Our findings open up novel scenarios for understanding the molecular mechanisms of PD.

Results and discussion

Characterization of iron-induced alpha synuclein aggregates

To test the effect of iron in promoting structural changes of αS we first performed the *in vitro* incubation of WT and A53T αS in the presence of $FeCl_2$ salt solution. As a reference we measured *via* dynamic-mode AFM imaging in air the morphology of WT and A53T αS monomers deposited on a mica substrate after 1 h shaking incubation of 35 μM αS in pure Milli-Q water (no iron cations) at 37 °C. Pure Milli-Q water was chosen to avoid any possible contribution from saline ions in the solution to the aggregation of monomeric αS. The αS concentration of 35 μM is matching the *in vivo* physiological concentration of αS (in the μM range[43]). From our images we found the presence of monomers and dimers with height in the range of 0.3–0.9 nm, in agreement with previous measurements *via* AFM[44] (Fig. 1A–C). In both cases we did not observe any formation of protein aggregates. Then we added 2 mM of Fe^{2+} to the solution containing 35 μM αS and shaken for 1 h in pure Milli-Q water at 37 °C, as before. We chose a Fe^{2+} concentration two orders of magnitude higher than the typical iron content inside a cell (50–100 μM)[45] to promote the aggregation of the proteins, as reported by Uversky *et al.* colleagues.[34] Our previous studies have shown that iron drives human WT αS to form oligomers with an average height of 4.0 nm.[46] Here, AFM images confirmed the formation of these globular protein

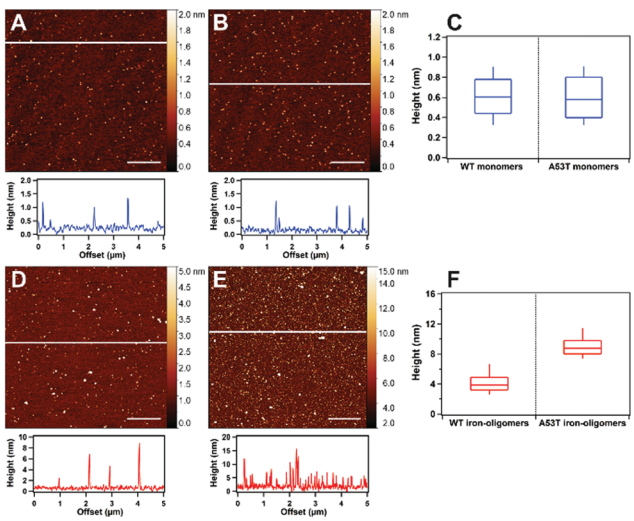

Fig. 1 AFM morphological analysis of human αS monomers and Fe^{2+}-mediated αS oligomers. (A) WT and (B) A53T αS monomeric species deposited on a sheet of mica with the relative profiles of height traced along the surface. (C) Box plot analysis of the height distribution of WT *vs.* A53T monomers. (D) WT and (E) A53T αS aggregates after iron treatment. (F) Box plot analysis of the height distribution of WT *vs.* A53T Fe^{2+} oligomers. Scale bar: 1 μm.

aggregates compatible with the presence of oligomeric species, both in the case of WT and A53T αS (Fig. 1D and E). In terms of height/morphology, A53T αS gives rise to a population of oligomers bigger than for the case of WT ones (mean height of 8.2 ± 1.4 nm for A53T *versus* 3.4 ± 1.2 nm in the case of WT αS, Fig. 1F). Sodium dodecyl sulphate-polyacrylamide gel electrophoresis (SDS-PAGE) and dynamic light scattering (DLS) measurements confirmed the trend observed by AFM (Fig. S1 and S2, ESI†). In particular, DLS pointed out the presence of particles with a hydrodynamic diameter of 5.6 ± 1.5 nm and 28.2 ± 5.0 nm for WT and A53T αS, respectively. The agreement between AFM (where proteins are trapped on a supporting surface) and DLS data (measured in solution) ruled out any effect of the mica surface in inducing protein aggregation.

Moreover, given the same protein reaction amount and reaction time, the measured 20-fold increase in the number of aggregates in the case of A53T specimen with respect of the WT αS (see Experimental), points to accelerated oligomerization kinetics for the mutant. Faster conversion of αS monomers into oligomers has been reported in the literature for some αS mutated species, as A53T and A30P, suggesting a critical role in the mutant-related PD pathology.[17,29]

αS-Oligomers are known to display different features in terms of dimensions (3–25 nm), morphology and types/amount of secondary structures, according to the different oligomerization conditions. They are usually classified into three categories: beta-sheet (β) enriched, mainly alpha (α)-helical and primary disordered oligomers.[47–49] To clarify the nature of our iron-induced protein aggregates, we ran FTIR-ATR measurements providing information about protein secondary structure. The Amide I band (1710–1580 cm^{-1}), mainly dominated by the C═O stretching vibration and directly related to the backbone conformation of the protein, showed a slight broadening both at higher and lower frequencies for the A53T αS compared to the WT protein (Fig. 2A, upper part). In both cases the main contributions appear at 1690 cm^{-1}, 1675 cm^{-1}, 1655 cm^{-1}, 1640 cm^{-1} and 1625 cm^{-1}, as picked out from the second derivative spectra (Fig. 2A, lower part). To evaluate the relative weight of such components, we performed a multi-peak Gaussian fitting of Amide I band (Fig. 2B and C). The major component of the band peaked at 1655 cm^{-1}, corresponding to the α-helix vibrational modes, is more pronounced in the case of WT αS (34% of the Amide I total area, with respect to 30% for the A53T). The contribution from the peak at 1640 cm^{-1}, related to the random coiled structures, slightly increase for the A53T αS (from 21.4% to 22.7%) suggesting a variation of the protein structural order if compared to the WT protein. Instead the components at 1690 and 1625 cm^{-1}, respectively attributed to the anti-parallel and parallel β-sheet structures, are more pronounced in the case of A53T αS: overall the WT αS aggregates display a β-sheet contribution of 18.3% (12.8% parallel and 5.5% antiparallel) of the total Amide I band, which increases to 22.4% (15.2% parallel and 7.2% antiparallel) in the case of A53T aggregates (Fig. 2D).[50]

It is well-known that the β-sheet conformation is predominant (>50%) in fibrils, and its percentage in weight raises progressively during the interconversion from monomers to amyloid fibrils.[51] The β-sheets state is therefore indicative of a proper structural organization of these aggregates. However, in a recent αS fibrillation assay, an involvement of α-helix intermediates during the aggregation process, proportional to the aggregation propensity of the specific αS specimen, has been demonstrated.[52] The percentage of β-sheets and α-helices found in our case (for both *wild-type* and A53T structures) is therefore compatible with the presence of early oligomers.

The idea that Fe^{2+} ions induce the formation of "early" oligomeric αS structures is also supported by recent AFM and Raman spectroscopy data showing that under specific conditions early-stage oligomers are primary α-helix, with a β-sheet content of around 29% at most and dimension very similar to the ones found in our aggregates.[53] Further, we hypothesize that the higher structural disorder might confer to A53T αS a more aggressive behaviour. The replacement of one alanine (A) with a bigger threonine (T) in fact might affect the αS structure conferring higher steric hindrance within the region around the mutation, affecting inter/intra molecular interactions.

In a recent replica exchange molecular dynamic simulations (REMD) study on both full-length monomeric WT and A53T αS, the stronger propensity of the A53T species to aggregate has also been related to the more abundant β-sheet content close to the mutation site in the N-terminal domain, and to the lack of strong intra-molecular long-range interactions in comparison to the WT αS, which leads to the overexposure of the NAC region to solvents.[54] In the presence of ferrous ions, as in our case, this increased exposure could contribute to a faster formation/higher aggressiveness of the A53T oligomers, and as a consequence to earlier development of the disease. Besides, particular mention has to be given to the metal-interacting sites on the sequence of αS. Most of essential metal ions bind the protein with a weak interaction at C-terminal domains, involving three aminoacidic residues, Asp121, Asn122 and Glu123. On the other hand, another residue (His50) has been proposed to be targeted by Fe-ions.[39]

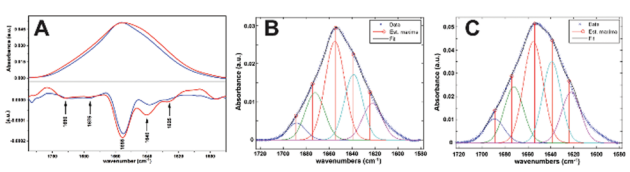

D

Wavelength (cm^{-1})	1690	1675	1655	1640	1625
Structural components (%)	Anti-parallel β-sheet	Turn-Loops	α-helix	Random coil	Parallel β-sheet
WT αS Fe^{2+}-oligomers	5.5	16.5	34.4	21.4	12.8
A53T αS Fe^{2+}-oligomers	7.2	16.7	30.5	22.7	15.2

Fig. 2 FTIR-ATR spectra of Fe^{2+}-mediated αS oligomers. (A) Comparative absorbance spectra of Amide I band of WT and A53T αS Fe^{2+}-oligomers with the respective second derivatives. FTIR deconvolution analysis (B) WT and (C) A53T Amide I band. Gaussian fitting was performed at 1690, 1675, 1655, 1640 and 1625 cm^{-1}. (D) Secondary structure contribution assigned to each fitted peak.

This site is very close to the mutation A53T, suggesting that this mutation could influence the effect of αS-iron binding in the aggregation and conformational change of the protein. Unfortunately, the structural and functional features of these Fe-binding site still lack a complete characterization.

Interaction of αS with raft-like model membranes

Once characterized the effect of iron on αS aggregation we moved on to study the interaction of monomers/oligomers with artificial cell membranes. Since the lipid rafts of the cell membrane are the key sites for biological and pathological functions of αS[9–12] we produced a supported planar lipid bilayer (SLB) with mixed lipid composition to reproduce raft-like molecular organization. We fabricated a ternary model membrane made by phosphatidylcholine (DOPC), sphingomyelin (SM) and cholesterol (Chol) which mimics the structure of neuronal membranes.[55] SM is known to organize in ordered, phase-separated domains, floating in the fluid matrix of the DOPC bilayer.[56] We chose to work with a relative DOPC : SM ratio of 66 : 33 (molar ratio), and 5% of cholesterol. Although cholesterol concentration in real cell membranes varies between the 15% and 50% of the total lipid composition, 5% cholesterol chosen here is enough to confer stability to the lipid rafts and to guarantee at the same time a contrast between the two phases, observable by AFM dynamic imaging in liquid environment. From AFM topography analysis we measured an extended phase attributed to a DOPC enriched bilayer with smaller domains that protrude out of it of 1.0 ± 0.2 nm (Fig. 3A–C). Such areas are assigned to SM and cholesterol-enriched domains in agreement with the differential height obtained by previous studies on one-component membranes showing thickness of about 5.0 nm for a fully hydrated DOPC bilayer on mica and of about 6.35 nm for a SM bilayer.[57,58] We also assigned the DOPC rich areas to the liquid-disordered/fluid phase (Lα) and the SM and Chol domains to the solid-ordered phase (So) in agreement with the relative 3-lipids phase diagram.[59] The quality of the bilayer is confirmed by the flatness of both phases (surface roughness: Lα = 0.16 ± 0.05 nm, So = 0.14 ± 0.05 nm) which excludes the presence of any intermediate phase or of poor assembly of the membrane. Further details on our biomimetic membranes are given in Fig. S3 and S4.†

With a reliable and reproducible model of a raft-like lipid bilayer in our hands, we challenged the system to compare the interaction of WT and A53T αS with the membrane in a physiological environment before and after the addition of iron. A great deal of experimental evidence indicates that membrane binding by monomeric αS induces a conformational transition of the protein into helical state by the first interaction of the N-terminal domain with the bilayer.[60] However, the interaction of the protein with planar phase-coexisting membranes still lacks robust data.

4.5 μM of protein monomers were initially incubated with the membrane while acquiring AFM images. The interaction was monitored continuously *versus* time. In the case of WT αS, after 30 min incubation the nucleation of defect islands with a fractal shape was observed in correspondence of the DOPC-enriched fluid phase only (Fig. 4A). The defects area increased with time, while the nucleation of new fractal nuclei was impaired (only one new island appeared in 160 min observation period). The specificity of the interaction of WT αS with DOPC lipid phase was confirmed by the time evolution of the areas occupied by the two lipid phases Lα and So, defined according to their AFM heights, compared to the image area

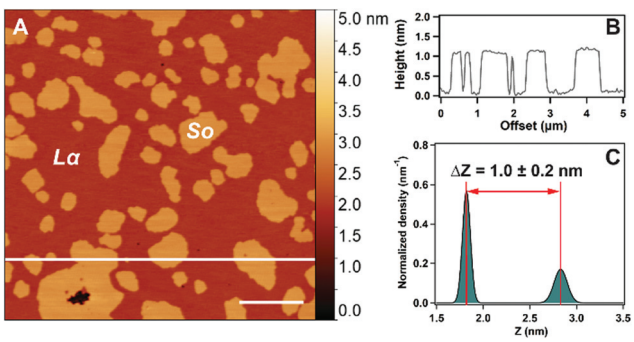

Fig. 3 Coexistence of liquid-disordered (Lα) and solid-ordered (So) phase in planar supported lipid bilayer mimicking raft-like domains. (A) AFM topography image of ternary SLB composed by DOPC, SM and cholesterol. Image was taken in aqueous buffer in dynamic AC-mode. Scale bar: 1.0 μm. (B) Section analysis (white line along the image) shows So-domains protruding from the fluid matrix (Lα) of SLB of ≈ 1.0 nm. (C) The height distribution explains the difference of thickness (ΔZ) between So and Lα lipid phases. Lα = liquid-disordered, So = solid-ordered.

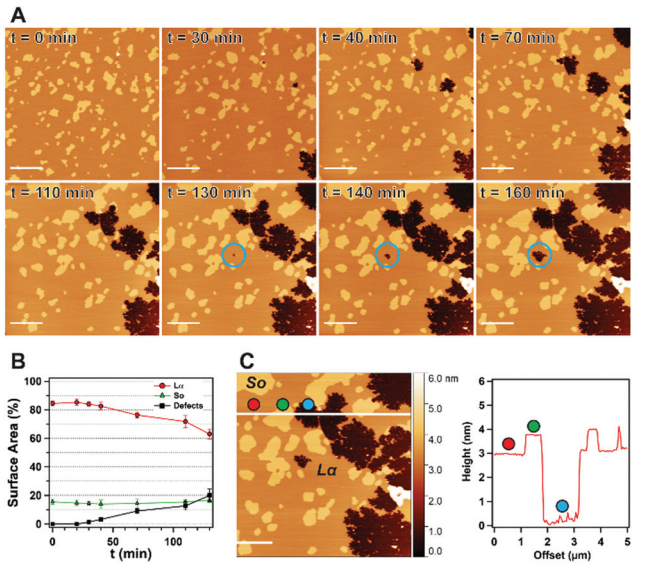

Fig. 4 Interaction of monomeric WT αS with SLB resembling raft-like domains. (A) AFM imaging over time of protein monomers interacting with DOPC/SM/Chol SLB. Blue circle indicates the formation of fractal-like defects. (B) Time-evolution of Lα, So and defects areas. (C) AFM image and the trace profile highlight the morphology/height of Lα phase (red ●), So-domains (green ●) and αS-inducing defects (light blue ●). Scale bar: 1 μm.

occupied by the fractal-like defects. The Lα phase area decreased from 85% to about 60% after 2 h of protein incubation while the defects area increased by up to 20%. On the contrary the area of the So raft-like domains stayed constant in time. The results are shown in Fig. 4B. The defect islands showed an average depth of 2.5 ± 0.4 nm for the DOPC phase. Such value matches the thickness of one single lipid layer in the bilayer structure (Fig. 4C). This is compatible with a lateral expansion of lipid molecules due to the interdigitation of the protein in the upper layer of the SLB which finally leads to membrane thinning. Overall our results indicate that monomeric WT αS interacts strongly with the DOPC headgroups promoting a reshape of the Lα phase. The average fractal dimension (D) of the growing defects was determined *via* box-counting methods. We found D = 1.77 ± 0.03, a value that falls within the range typical of diffusion limited-reaction processes (*i.e.*, where diffusion time dominates over reaction time).[61,62]

When we moved to mutated A53T αS, we observed the formation of defect islands more ring-shaped compared to the WT case, as confirmed by the higher fractal dimension (D = 1.86 ± 0.02). Islands grew in size *versus* time and propagated within the DOPC layer, starting from the boundaries between the Lα phase and the So-domains (Fig. 5A).

The average defect deepness of 2.4 ± 0.5 nm is compatible with the dimension of half a bilayer, as for the case of WT αS. However, the growth of the A53T-related defects proceeded faster than for WT αS, covering 40% of the total area after 2 h of protein incubation (Fig. 5B). Fig. 5C shows the comparison of the growth of single defect domains area *versus* time in case of WT and A53T αS. The mutant form, being 4-fold faster than WT αS, points, therefore, to a different membrane-interaction kinetics. In the phase-coexisting membranes reported here, the protein in monomeric form (both WT and A53T) find then more accessible the Lα phase of the bilayer with respect to the raft-like domains, inducing a reorganization of membrane structure *via* a thinning of the bilayer. A similar effect was observed by our group in a previous work, in the case of WT αS in interaction with one-component (DOPC) SLB.[46] However, the two monomeric proteins show different interaction kinetics: at equal concentration the mutant A53T αS is faster than the WT protein in targeting the membrane. Other studies reported a membrane thinning effect by αS, a process that has been demonstrated crucial *in vivo* for protein-regulated vesicle trafficking, and that has to have implications in the onset of PD disease.[63] Also, similar interaction mechanisms are shared with other membrane-interacting proteins as antimicrobial peptides.[64–66]

When the raft-like supported lipid bilayers were placed in interaction with the WT αS-aggregates obtained by incubation with Fe^{2+} we observed protein clusters accumulating on the bilayer surface. AFM images acquired continuously for 90 minutes revealed that such oligomers are always located in the proximity of the So phase, highlighting a preferential interaction with the LR domains (Fig. 6A). Oligomers accumulation did not involve all LR domains. The nucleation is followed by a growth process with the formation of clusters that, in a small

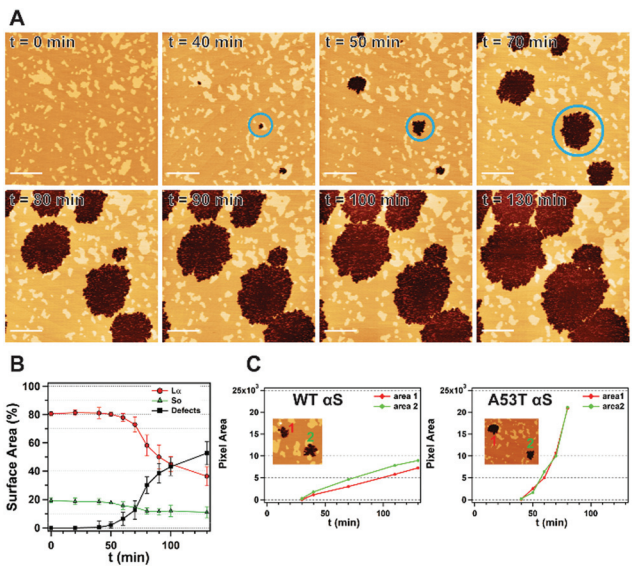

Fig. 5 Interaction of monomeric A53T αS with SLB resembling raft-like domains. (A) AFM imaging over time of protein monomers interacting with DOPC/SM/Chol SLB. Blue circle indicates the formation of fractal-like defects. Scale bar: 1 μm. (B) Relative change of Lα, So and αS-inducing defects areas *vs.* time. (C) Analysis of growth of singular fractal-like defects of WT and A53T αS.

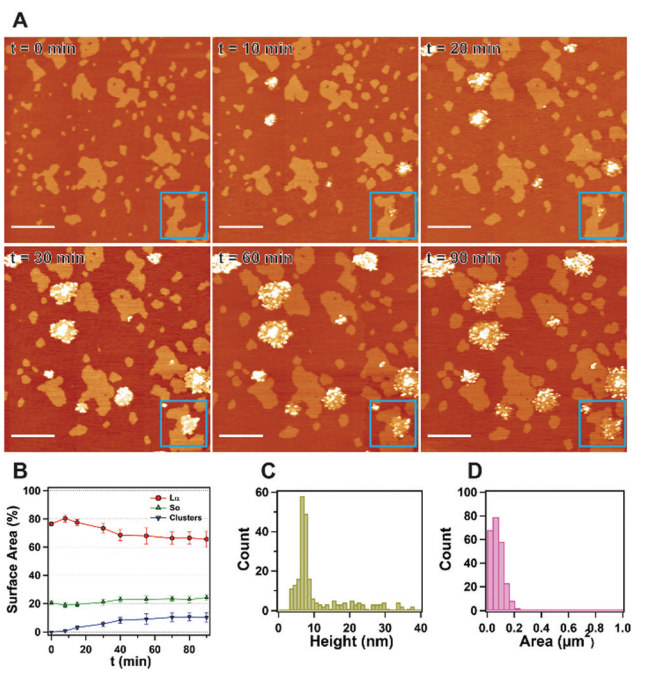

Fig. 6 Interaction of iron-induced WT αS oligomers with raft-like SLB. (A) AFM topographic images of membrane-protein interaction monitored over time. Blue squares point the nucleation of oligomers on the So-domains and its time-evolution. Scale bar: 1 μm. (B) Analysis of relative surface areas of Lα, So and oligomeric clusters *vs* time. Distribution of (C) heights and (D) areas of clusters.

portion, extend to the adjacent Lα phase of the bilayer (Fig. 6B).

From AFM morphological analysis, we see that these globular aggregates have 200–600 nm lateral dimension and surface areas up to 0.2 μm^2, protruding by 6.4 ± 1.4 nm from the LR domains (Fig. 6C and D).

Finally, the incubation of Fe^{2+}-promoted A53T mutant aggregates on our SLB displayed similar results. Globular clusters of aggregated oligomers were initially interacting with the SLB So phase only (Fig. 7A), soon spreading onto the fluid phase of the bilayer as for the WT aggregates. The main difference between WT and A53T αS oligomers resides in the kinetics of interaction with the bilayer. The mutant A53T aggregates interact faster with the bilayer forming larger clusters that cover the 50% of the bilayer after 90 minutes of incubation, 5-fold time faster compared to the WT oligomers (Fig. 7B).

The morphology of these clusters reflects the propensity of the protein to form larger oligomers upon Fe^{2+} treatment, as described in Fig. 1, before interacting with the membrane. Also, they have a 2-fold lateral dimensions (up to 1400 nm) and 2-fold height dimension (a heterogeneous distribution in the of 10–30 nm) compared to WT αS clusters (Fig. 7C and D). We can conclude here that, at variance with iron-aggregated WT αS oligomers on single-phase (DOPC) SLB which have been shown to accumulate on the fluid membrane forming protein clusters,[46] on mixed-phase bilayers oligomers eventually interact with both the Lα-fluid and So-ordered phase of the membrane, being the nucleation process triggered and favored by the sole So-domains.

FTIR-ATR measurements were performed to gain more structural insights on the protein-membrane interaction. We incubated the Fe^{2+}-mediated oligomers with large unilamellar vesicles (LUVs) of the same lipid composition of the SLB used in the AFM experiments. Due to the large surface tension LUVs opened up when deposited on the ATR crystal forming a lipid bilayer (see Experimental). In Fig. 8A, the spectra of the bare membrane with and without Fe^{2+} were compared with the ones corresponding to Fe^{2+}-mediated oligomers of both proteins incubated with the vesicles in the range of 1800–700 cm^{-1}, covering both amine I and phospholipid vibrational bands.

The main spectral difference was observed in the region 1330–1150 cm^{-1}, dominated by the absorption peak of the $(-PO_2)^-$ asymmetric stretching mode (Fig. 8B). Interestingly, the Fe^{2+}-A53T αS aggregates/membrane peak shape is similar to the one recorded for the bare membrane; likewise, a close similarity was observed for the broad Fe^{2+}-WT αS oligomers/membrane and the Fe^{2+}/membrane spectra. We assume that the shift and broadening of these last two peaks might be due to the formation of complexes between iron ions and the phosphates headgroups of the lipids.[67] This implies a low binding affinity of Fe^{2+} for the WT αS oligomers. Fe^{2+} is sequestered by the lipids of the bilayer and interacts with lipid headgroups.

On the contrary, the peak shape similarity between Fe^{2+}-A53T αS aggregates/membrane and membrane alone (the first being slightly shifted to lower wavenumbers) suggests a stronger interaction of the mutated protein with Fe^{2+} in the aggregates. This is in line with the higher β-sheet content found for A53T with respect to WT αS oligomers, shown in Fig. 2, which points towards a higher aggressiveness of the first ones and with our AFM imaging data, *i.e.* a faster kinetics of interaction of A53T αS oligomers with the membrane and the formation of larger clusters, also confirmed by other groups.[42]

In this case, the major part of the iron ion is probably involved in the formation of the oligomers of the mutated

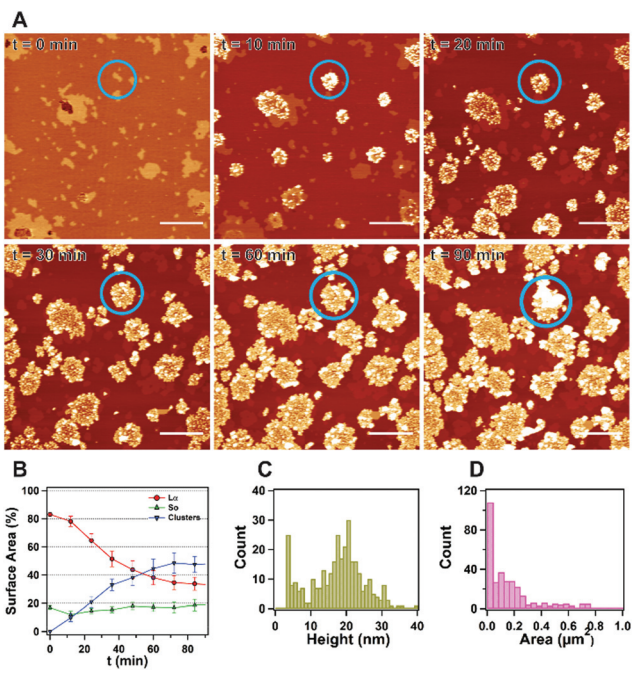

Fig. 7 Interaction of iron-induced A53T αS oligomers with raft-like SLB. (A) AFM topographic images of membrane-protein interaction monitored over time. Blue circles show the nucleation of oligomers on the So-domains and its time-evolution. Scale bar: 1 μm. (B) Analysis of relative surface areas of Lα, So and oligomeric clusters *vs* time. Distribution of (C) heights and (D) areas of clusters.

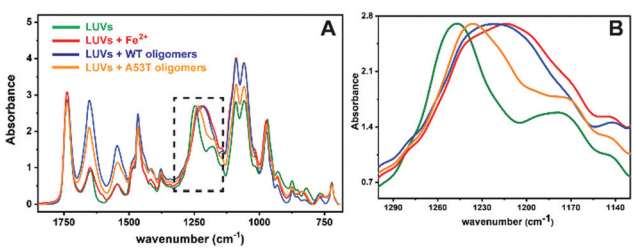

Fig. 8 FTIR-ATR measurements of the interaction between iron-mediated oligomers with LUVs resembling raft-like membrane organization. (A) Absorbance spectra of LUVs-WT αS oligomers (blue), LUVs-mutant A53T oligomers (orange), lipid membrane (dark green) and lipid membrane incubated with Fe^{2+} (red). (B) The comparative analysis showed the main difference in the region of phosphate group stretching (1330–1150 cm^{-1}), revealing a different behavior of the proteins in the binding of the metal.

A53T αS and thus, not available for interacting with the membrane.

Conclusion

In conclusion we proposed here a novel approach based on AFM and FTIR measurements, which focuses on the interaction between iron-induced αS aggregates and the different lipid phases of an artificial supported lipid bilayer mimicking the composition of neuronal membranes. The binding of misfolded protein oligomers to biological membranes is considered one of the key molecular events at the basis of the pathological development and progression of many neurodegenerative disease, such as PD.[19] Here, working at the submicrometric level we demonstrated the ability of ferrous cations to promote strong and fast *in vitro* aggregation of both WT and mutant A53T αS, leading to the formation of early stage oligomers. We proved that distinct monomeric and oligomeric αS species interact in a different way with the fluid lipid phase and the raft-like lipid nanostructures: αS monomers cause membrane thinning while the iron-mediated αS oligomers studied here do not produce any similar impairment of the membrane. Instead, we observed the accumulation of the metal-promoted aggregates on LR-like domains strengthening the hypothesis of a critical role of LRs in the development and progression of the disease. Accumulation of iron in the brain, which is peculiar of the PD pathology, is then promoting the formation of αS-oligomers, which accumulate on LR-domains of plasma membranes. This in turn alters the membrane affecting a plethora of biological processes regulated by signaling membrane proteins localized in the rafts, firstly the homeostasis of neurotransmitter exocytosis.[68] A similar scenario has been reported for the Aβ-peptide in AD, in which lipid rafts are promoting the aggregation of Aβ-peptide that in turn, by clustering specific raft-proteins, lead an impairment of raft-molecular pathways contributing to neurotoxicity.[69,70] The critical role played by lipid rafts in the interaction with amyloid protein oligomers is essential for understanding the development and progression of PD and ultimately for developing therapies targeting LR components.

Experimental

Materials

18 : 1 (Δ9-Cis) PC (1,2-dioleoyl-*sn-glycero*-3-phosphocholine, DOPC), sphingomyelin (brain, porcine, SM) and cholesterol (ovine wool, >98%) were purchased by Avanti polar lipids (Alabaster, USA). $FeCl_2$ solution was prepared by dissolving salt powder (Sigma Aldrich) in ultrapure 18.2 MΩ cm water (Milli-Q, Millipore SpA, Milan, Italy) and filtered with a sterile syringe-filter (0.22 μm) prior to use. Expression and purification of human *wild-type* alpha synuclein (WT αS) and human mutated A53T αS was performed by the group of Prof. Giuseppe Legname (Laboratory of Prion Biology, SISSA – Scuola Internazionale Superiore di Studi Avanzati, Trieste, Italy) according to the method of Huang *et al.* colleagues.[71]

Lipid vesicles preparation and supported lipid bilayer formation

For the production of supported lipid bilayer (SLB) by vesicle fusion we have followed the procedure described by Oropesa-Nuñez and colleagues.[72] Briefly, DOPC, SM and cholesterol powders were dissolved in chloroform at the final concentration of 1 mg mL^{-1}. Lipid solution were used to produce a lipid mixture made by DOPC/SM (66 : 33 in molar ratio) + 5% cholesterol (molar) which was gently evaporated under a stream of nitrogen. Samples were placed under vacuum overnight in order to completely removed solvent residues and resuspended in Milli-Q water at a lipid concentration of 1 mg mL^{-1} to form multilamellar vesicles (MLVs). MLVs were left to swell for 1 h at 60 °C and then extruded 51 times through a polycarbonate membrane with 100 nm pores using a commercial extruder (Avanti Polar Lipids) at the same temperature, to form large unilamellar vesicles (LUVs). After cooling at room temperature, LUVs were diluted 10-fold with Milli-Q water. Then, 90 μL of LUVs suspension and 10 μL of a 50 mM $CaCl_2$ solution were deposited onto a 1.0 cm × 1.0 cm of freshly cleaved mica substrate attached to the AFM liquid chamber by ultrafast glue. The samples were stored 15 min at room temperature to promote LUVs rupture and fusion on mica surface, in order to produce uniform lipid bilayer. Then the AFM chamber was completely filled with Milli-Q water and, after 1 h, membrane was gently rinsed three times with Milli-Q water to remove excess vesicles from the liquid sub-phase before AFM measurements.

In vitro aggregation of αS

In order to study iron-mediated aggregation of human WT αS and the mutant A53T αS, 100 μg of each αS protein (final concentration: 35 μM) were mixed with 2 mM $FeCl_2$. Protein solutions were incubated at 37 °C under shaking for 1 hour. 10 μL of protein solution were spread onto 1.0 cm × 1.0 cm piece of freshly cleaved mica, left to incubate for 5 min, gently rinsed 3 times with Milli-Q water, dried with a stream of nitrogen, and successively analyzed by AFM in air at room temperature.

Atomic force microscopy (AFM) imaging

All AFM images were acquired using a commercially available microscope (MFP-3D Stand Alone AFM from Asylum Research, Santa Barbara, CA). Measurements were carried out at room temperature working in dynamic AC-mode. Commercially available silicon cantilevers (OMCL-RC800PSA-1, Olympus Micro Cantilevers, nominal spring constant 0.76 nN nm^{-1},) have been chosen for imaging in liquid. High resolution images (512 × 512 pixels frames) were acquired at 0.6–1 lines per s scan speed. For studying αS interaction with raft-like membranes, 100 μg of iron-induced oligomers and protein monomers of human *wild-type* αS and A53T mutant αS (35 μM) were incubated to supported lipid bilayer for 1 h at room temperature (final protein concentration 4.5 μM) and imaged by

AFM. AFM images were analyzed using Gwyddion, open-source modular program for scanning probe microscopy (SPM) data visualization and analysis.[73] Time-evolution analysis of the relative areas of Lα phase, So phase and αS defects/clusters were expressed as mean ± standard deviation (SD) obtained from three independent experiments (n = 3) for each condition. Surface roughness of Lα and So lipid phases was determined as R_{ms} value of the height irregularities. Height distribution was fitted using a double Gaussian function using Igor Pro software (Wavemetrics, US). For the analysis of the number and size distribution of αS aggregates the grain analysis macro of Gwyddion software was used. The 20 fold-increase of A53T Fe^{2+}-oligomers *vs.* WT protein was obtained calculating the number of protein particles and normalizing with the number of analyzed images (n = 10).

FTIR-ATR spectroscopy

All the Infrared measurements were performed at the Chemical and Life Sciences branch of SISSI (Synchrotron Infrared Source for Spectroscopy and Imaging, Elettra-Sincrotrone Beamlines, Basovizza, Trieste, Italy). For the first experiment, 10 μg of iron-induced oligomers of human WT αS and the mutant A53T species were diluted in 200 μL of Milli-Q water. For the second experiment 60 μg of LUVs composed by DOPC/SM (66 : 33) + 5% cholesterol were mixed with 10 μg of Fe^{2+}-induced oligomers of both proteins, and incubated for 1 h at room temperature. For the control, 60 μg of LUVs were incubated in Milli-Q water or 0.2 mM $FeCl_2$ salt solution for 1 h at room temperature. For each experiment, 200 μL of sample solution were spread over the whole area of a trapezoidal germanium multiple ATR crystal and left to dry forming a thin film of the sample. The crystal is 50 mm × 10 mm × 2 mm wide with an incidence angle of 45° yielding 25 internal reflections. Infrared analyses were performed by using the off-line Bruker Vertex 70 interferometer equipped with RT-DLaTGS detector. 30 consecutive spectra were acquired for monitoring the complete drying of the sample. Every spectrum was collected at 2 cm^{-1}, repeating 256 scans in the range 4500–800 cm^{-1}. The data-set was pre-processed with Bruker software OPUS 7.5. The spectra were first baseline corrected in the 4000–800 cm^{-1} spectra region (rubberband correction algorithm, 64 points) and then cut into two regions of interest: ROI 1, Amide I region, (1750–1580 cm^{-1}, Fig. 3); ROI 2, phosphates bands (1330–1150 cm^{-1}, Fig. 8). Spectra were then further baseline corrected, (rubberband method, 16 points) and normalized to the same height with a Min/Max function in order to better compare the band shapes among them and highlight the differences in their infrared features. The spectra in the selected ROI were plotted by OriginPro 8 software and second derivatives were computed for the Amide I band by applying the Savitzky–Golay method with 9 smoothing points (OriginPro2018 – Originlab) in order to better observe the overlapped sub-bands. They have been used as input parameters for the-multi-peak fitting performed by a Matlab in-house written routine.[74] During fitting, the peak positions have been let to vary by ±2 cm^{-1}, while FWHM between 5 to 20 cm^{-1}. The percentage area of each Gaussian has been calculated on the total area of the Amide I band.

Conflicts of interest

There are no conflicts to declare.

Acknowledgements

L. C., D. S. and F. P. acknowledge support by the Italian Health Ministry (GR-2011-02348707). L. C., P. P. and F. P. acknowledge also CERIC-ERIC proposal grant no. 20167068 to perform measurements at the Chemical and Life Sciences branch of SISSI (Synchrotron Infrared Source for Spectroscopy and Imaging, Elettra-Sincrotrone Beamlines, Basovizza, Trieste, Italy). G. L. acknowledges intramural SISSA funding supporting this work.

Notes and references

1 M. Goedert, *Nat. Rev. Neurosci.*, 2001, **2**, 492.
2 M. G. Spillantini, M. L. Schmidt, V. M.-Y. Lee, J. Q. Trojanowski, R. Jakes and M. Goedert, *Nature*, 1997, **388**, 839.
3 M. Stöckl, M. M. A. E. Claessens and V. Subramaniam, *Mol. BioSyst.*, 2012, **8**, 338.
4 J. P. Segrest, M. K. Jones, H. De Loof, C. G. Brouillette, Y. V. Venkatachalapathi and G. M. Anantharamaiah, *J. Lipid Res.*, 1992, **33**, 141.
5 M. Bisaglia, E. Schievano, A. Caporale, E. Peggion and S. Mammi, *Biopolymers*, 2006, **84**, 310.
6 A. M. Bodles, D. J. Guthrie, B. Greer and G. B. Irvine, *J. Neurochem.*, 2001, **78**, 384.
7 B. I. Giasson, I. V. J. Murray, J. Q. Trojanowski and V. M.-Y. Lee, *J. Biol. Chem.*, 1999, **274**, 7619.
8 I. V. J. Murray, B. I. Giasson, S. M. Quinn, V. Koppaka, P. H. Axelsen, H. Ischiropoulos, J. Q. Trojanowski and V. M. Lee, *Biochemistry*, 2003, **42**, 8530.
9 D. Scott and S. Roy, *J. Neurosci.*, 2012, **32**, 10129.
10 J. Burré, M. Sharma and T. C. Südhof, *Proc. Natl. Acad. Sci. U. S. A.*, 2014, **111**, E4274.
11 J. Burré, M. Sharma, T. Tsetsenis, V. Buchman, M. R. Etherton and T. C. Sudhof, *Science*, 2010, **329**, 1663.
12 D. L. Fortin, M. D. Troyer, K. Nakamura, S. Kubo, M. D. Anthony and R. H. Edwards, *J. Neurosci.*, 2004, **24**, 6715.
13 J. Eschbach and K. M. Danzer, *Neurodegener. Dis.*, 2014, **14**, 1.
14 A. C. Hoffmann, G. Minakaki, S. Menges, R. Salvi, S. Savitskiy, A. Kazman, H. V. Miranda, D. Mielenz, J. Klucken, J. Winkler and W. Xiang, *Sci. Rep.*, 2019, **9**, 544.

15 C. R. Pacheco, C. N. Morales, A. E. Ramírez, F. J. Muñoz, S. S. Gallegos, P. A. Caviedes, L. G. Aguayo and C. M. Opazo, *J. Neurochem.*, 2015, **132**, 731.
16 B. Winner, R. Jappelli, S. K. Maji, P. A. Desplats, L. Boyer, S. Aigner, C. Hetzer, T. Loher, M. Vilar, S. Campioni, C. Tzitzilonis, A. Soragni, S. Jessberger, H. Mira, A. Consiglio, E. Pham, E. Masliah, F. H. Gage and R. Riek, *Proc. Natl. Acad. Sci. U. S. A.*, 2011, **108**, 4194.
17 K. A. Conway, S. J. Lee, J. C. Rochet, T. T. Ding, R. E. Williamson and P. T. Lansbury, *Proc. Natl. Acad. Sci. U. S. A.*, 2000, **97**, 571.
18 M. Ingelsson, *Front. Neurosci.*, 2016, **10**, 408.
19 M. Andreasen, N. Lorenzen and D. Otzen, *Biochim. Biophys. Acta, Biomembr.*, 2015, **1848**, 1897.
20 B. D. van Rooijen, M. M. A. E. Claessens and V. Subramaniam, *Curr. Protein Pept. Sci.*, 2010, **11**, 334.
21 H.-Y. Kim, M. K. Cho, A. Kumar, E. Maier, C. Siebenhaar, S. Becker, C. O. Fernandez, H. A. Lashuel, R. Benz, A. Lange and M. Zweckstetter, *J. Am. Chem. Soc.*, 2009, **131**, 17482.
22 C. Pacheco, L. G. Aguayo and C. Opazo, *Front. Physiol.*, 2012, **3**, 297.
23 K. M. Danzer, D. Haasen, A. R. Karow, S. Moussaud, M. Habeck, A. Giese, H. Kretzschmar, B. Hengerer and M. Kostka, *J. Neurosci.*, 2007, **27**, 9220.
24 L. J. Hsu, Y. Sagara, A. Arroyo, E. Rockenstein, A. Sisk, M. Mallory, J. Wong, T. Takenouchi, M. Hashimoto and E. Masliah, *Am. J. Pathol.*, 2000, **157**, 401.
25 E. Carboni and P. Lingor, *Metallomics*, 2015, **7**, 395.
26 K.-P. Wu, D. S. Weinstock, C. Narayanan, R. M. Levy and J. Baum, *J. Mol. Biol.*, 2009, **391**, 784.
27 A. M. Helferich, P. J. McLean, J. H. Weishaupt and K. M. Danzer, *J. Neurol. Neuromedicine*, 2016, **1**, 28.
28 M. H. Polymeropoulos, C. Lavedan, E. Leroy, S. E. Ide, A. Dehejia, A. Dutra, B. Pike, H. Root, J. Rubenstein, R. Boyer, E. S. Stenroos, S. Chandrasekharappa, A. Athanassiadou, T. Papapetropoulos, W. G. Johnson, A. M. Lazzarini, R. C. Duvoisin, G. Di Iorio, L. I. Golbe and R. L. Nussbaumet, *Science*, 1997, **276**, 2045.
29 K. A. Conway, J. D. Harper and P. T. Lansbury, *Nat. Med.*, 1998, **4**, 1318.
30 W. Choi, S. Zibaee, R. Jakes, L. C. Serpell, B. Davletov, R. A. Crowther and M. Goedert, *FEBS Lett.*, 2004, **576**, 363.
31 P. Riederer, E. Sofic, W. D. Rausch, B. Schmidt, G. P. Reynolds, K. Jellinger and M. B. Youdim, *J. Neurochem.*, 1989, **52**, 515.
32 J. M. Gorell, C. C. Johnson, B. A. Rybicki, E. L. Peterson, G. X. Kortsha, G. G. Brown and R. J. Richardson, *Neurotoxicology*, 1999, **20**, 239.
33 J. M. Gorell, B. A. Rybicki, C. C. Johnson and E. L. Peterson, *Neuroepidemiology*, 1999, **18**, 303.
34 V. N. Uversky, J. Li and A. L. Fink, *J. Biol. Chem.*, 2001, **276**, 44284.
35 D. T. Dexter, F. R. Wells, A. J. Lees, F. Javoy-Agid, Y. Agid, P. Jenner and C. D. Marsden, *J. Neurochem.*, 1989, **52**, 1830.
36 E. C. Hirsch, J. P. Brandel, P. Galle, F. Javoy-Agid and Y. Agid, *J. Neurochem.*, 1991, **56**, 446.
37 D. T. Dexter, A. Carayon, F. Javoy-Agid, Y. Agid, F. R. Wells, S. E. Daniel, A. J. Lees, P. Jenner and C. D. Marsden, *Brain*, 1991, **114**, 1953.
38 V. N. Uversky, J. Li and A. L. Fink, *J. Biol. Chem.*, 2001, **276**, 10737.
39 A. Binolfi, R. M. Rasia, C. W. Bertoncini, M. Ceolin, M. Zweckstetter, C. Griesinger, T. M. Jovin and C. O. Fernández, *J. Am. Chem. Soc.*, 2006, **128**, 9893.
40 K. Li and H. Reichmann, *J. Neural Transm.*, 2016, **123**, 389.
41 R. Ortega, A. Carmona, S. Roudeau, L. Perrin, T. Dučić, E. Carboni, S. Bohic, P. Cloetens and P. Lingor, *Mol. Neurobiol.*, 2016, **53**, 1925.
42 N. Ostrerova-Golts, L. Petrucelli, J. Hardy, J. M. Lee, M. Farer and B. Wolozin, *J. Neurosci.*, 2000, **20**, 6048.
43 R. Borghi, R. Marchese, A. Negro, L. Marinelli, G. Forloni, D. Zaccheo, G. Abbruzzese and M. Tabaton, *Neurosci. Lett.*, 2000, **287**, 65.
44 F. S. Ruggeri, F. Benedetti, T. P. J. Knowles, H. A. Lashuel, S. Sekatskii and G. Dietler, *Proc. Natl. Acad. Sci. U. S. A.*, 2018, **115**, 7230.
45 O. Kakhlon and Z. I. Cabantchik, *Free Radicals Biol. Med.*, 2002, **33**, 1037.
46 F. Perissinotto, V. Rondelli, P. Parisse, N. Tormena, A. Zunino, L. Almásy, D. G. Merkel, L. Bottyán, Sz. Sajti and L. Casalis, *Biophys. Chem.*, 2019, **255**, 106272.
47 N. Cremades, S. W. Chen and C. M. Dobson, *Int. Rev. Cell Mol. Biol.*, 2017, **329**, 79.
48 D.-P. Hong, S. Han, A. L. Fink and V. N. Uversky, *Protein Pept. Lett.*, 2011, **18**, 230.
49 L. Breydo and V. N. Uversky, *FEBS Lett.*, 2015, **589**, 2640.
50 S. J. Roeters, A. Iyer, G. Pletikapiä, V. Kogan, V. Subramaniam and S. Woutersen, *Sci. Rep.*, 2017, **7**, 41051.
51 B. H. Meier and A. Böckmann, *Curr. Opin. Struct. Biol.*, 2015, **30**, 43.
52 D. Ghosh, P. K. Singh, S. Sahay, N. N. Jha, R. S. Jacob, S. Sen, A. Kumar, R. Riek and S. K. Maji, *Sci. Rep.*, 2015, **5**, 9228.
53 M. M. Apetri, N. C. Maiti, M. G. Zagorski, P. R. Carey and V. E. Anderson, *J. Mol. Biol.*, 2006, **355**, 63.
54 O. Coskuner and O. Wise-Scira, *ACS Chem. Neurosci.*, 2013, **4**, 1101.
55 A. S. B. Olsen and N. J. Færgeman, *Open Biol.*, 2017, **7**, 170069.
56 N. Kahya, D. Scherfeld, K. Bacia, B. Poolman and P. Schwille, *J. Biol. Chem.*, 2003, **278**, 28109.
57 S. Attwood, Y. Choi and Z. Leonenko, *Int. J. Mol. Sci.*, 2013, **14**, 3514.
58 G. G. Shipley, L. S. Avecilla and D. M. Small, *J. Lipid Res.*, 1974, **15**, 124.
59 S. L. Veatch and S. L. Keller, *Phys. Rev. Lett.*, 2005, **94**, 148101.
60 T. S. Ulmer, A. Bax, N. B. Cole and R. L. Nussbaum, *J. Biol. Chem.*, 2005, **280**, 9595.

61 T. A. Witten and L. M. Sander, *Phys. Rev. Lett.*, 1981, **47**, 1400.
62 J. M. Moran-Mirabal, D. M. Aubrecht and H. G. Craighead, *Langmuir*, 2007, **23**, 10661.
63 Z. Shi, J. N. Sachs, E. Rhoades and T. Baumgart, *Phys. Chem. Chem. Phys.*, 2015, **17**, 15561.
64 W.-C. Hung, F.-Y. Chen, C.-C. Lee, Y. Sun, M.-T. Lee and H. W. Huang, *Biophys. J.*, 2008, **94**, 4331.
65 G. R. Heath, P. L. Harrison, P. N. Strong, S. D. Evans and K. Miller, *Soft Matter*, 2018, **14**, 6146.
66 F.-Y. Chen, M.-T. Lee and H. W. Huang, *Biophys. J.*, 2003, **84**, 3751.
67 H. Binder, K. Arnold, A. S. Ulrich and O. Zschörnig, *Biophys. Chem.*, 2001, **90**, 57.
68 T. Lang, *J. Physiol.*, 2007, **585**, 693.
69 I. Morgado and M. Garvey, *Adv. Exp. Med. Biol.*, 2015, **855**, 67.
70 J. V. Rushworth and N. M. Hooper, *Int. J. Alzheimers. Dis.*, 2010, **2011**, 603052.
71 C. Huang, G. Ren, H. Zhou and C. Wang, *Protein Expression Purif.*, 2005, **42**, 173.
72 R. Oropesa-Nuñez, S. Seghezza, S. Dante, A. Diaspro, R. Cascella, C. Cecchi, M. Stefani, F. Chiti and C. Canale, *Oncotarget*, 2016, **7**, 44991.
73 D. Nečas and P. Klapetek, *Open Phys.*, 2012, **10**, 181.
74 F. Cervelli, S. Carrato, A. Mattei, L. Benevoli and L. Vaccari, in Proc. 2012 20th European Signal Processing Conference (EUSIPCO), Bucharest, Romania, 2012.